Int. J. Electrochem. Sci., 15 **(2020)** 8563 – 8583, doi: 10.20964/2020.09.48

International Journal of
ELECTROCHEMICAL
SCIENCE
www.electrochemsci.org

Effect of Current Density on the Performance of Ni–Fe–P–CeO$_2$ Composite Coating Prepared by Jet Electrodeposition

Ren An-hua[1], *Fu Xiu-qing*[1, 2,*], *Duan Shuang-lu*[1], *Shen Mo-qi*[1], *Lin Jin-ran*[1]

[1] College of Engineering, Nanjing Agricultural University, Nanjing 210031, P. R. China;
[2] Key laboratory of Intelligence Agricultural Equipment of Jiangsu Province, Nanjing 210031, P. R. China;
[*]E-mail: fuxiuqing@njau.edu.cn

Received: 16 April 2020 / *Accepted:* 6 July 2020 / *Published:* 10 August 2020

To fabricate metal matrix composites with excellent performance, Ni–Fe–P–CeO$_2$ composite coating were prepared using jet electrodeposition technology at different processing current densities. The surface morphology, microstructure, and composition of the composite coatings were tested using scanning electron microscopy, energy dispersive X-ray spectroscopy, and X-ray diffractometry, respectively. The coatings were subjected to friction, wear, and corrosion tests to explore the effect of current density on the coating performance. The results showed that with the increase in the current density, the microhardness, wear resistance, and corrosion resistance of the amorphous composite coatings first increased and then decreased. When the current density was 30 A/dm^2, the surface smoothness of the composite coating was the best, the surface compactness was good, the microhardness was maximum (614.24 HV$_{0.1}$), and the coating surface exhibited excellent wear and corrosion resistances.

Keywords: Jet electrodeposition; Current density; Ni–Fe–P–CeO$_2$ composite coating; Wear resistance; Corrosion resistance

1. INTRODUCTION

A metal matrix composite (MMC) is a second-phase reinforced-composite material [1-3]. It can be prepared with a metal or an alloy matrix from a material having excellent mechanical properties and reliability in a wide range of engineering applications [4]. The performance of an MMC coating can be significantly improved by incorporating nanoparticles into the metal matrix[5,6], in terms of the hardness, wear resistance, strength, scratch resistance, high-temperature corrosion protection, oxidation resistance, and self-lubrication [7,8].

In the preparation of MMCs, jet electrodeposition is a convenient, fast, and inexpensive method for preparing composite coatings on the substrate surface [9-11]. The composition of the plating solution, plating process conditions, and nature of the particles incorporated affect the coating performance [12]. In recent years, nickel-based alloys have received much attention owing to their good wear and corrosion resistances [13-15]. Xiang [16] employed CeO_2 as an additive in SiC-modified, electrodeposited Ni–Fe alloy coatings to enhance the corrosion resistance and microhardness of the coating. Wang [17] prepared Ni–CeO_2 nanocomposite coatings using interlaced jet electrodeposition to improve the corrosion resistance. Sen [18] explored the effects of duty cycle on the microstructure and microhardness of a nano-Ni–CeO_2 composite coating prepared by pulse electrodeposition. Many studies have been conducted on nickel-based alloy coatings on binary alloys, but only few on ternary alloy coatings [19]. As active rare earth elements, nano-CeO_2 particles have the effects of modification, refinement, and alloying [20-24]. Aruna [25] reported that embedded CeO_2 particles are beneficial to the microhardness and protective properties of an Ni matrix.

The above studies indicate that an Ni–Fe–P–CeO_2 ternary alloy-based composite coating prepared by incorporating nano-CeO_2 particles into the nickel–iron matrix could exhibit excellent performance. In this study, a low-cost and easy-to-process #45 steel was selected as the matrix material. The jet electrodeposition technology was applied to add nano-CeO_2 particles as a reinforcing material to the plating solution. Fe and Ni were added as alloying elements into the #45 steel matrix to prepare an Ni–Fe–P–CeO_2 composite coating. The effects of processing current density on the surface morphology, microhardness, composition, wear resistance, and corrosion resistance of the Ni–Fe–P–CeO_2 composite coating were evaluated. Finally, the current density at which the coating exhibits the best performance was determined.

2. EXPERIMENTAL

2.1. Sample preparation and electrodeposition

The test base material was #45 steel (25 mm × 10 mm × 8 mm). Table 1 lists the composition of the plating solution. The reagents used were all analytically pure and prepared with deionized water. The substrate workpiece was polished with $800^{\#}$ and $1200^{\#}$ sandpaper successively, pre-treated before jet electrodeposition, including electric net degreasing, weak activation, and strong activation (each step took 20–30 s), and finally rinsed with deionized water after completion. The pre-treated workpiece was clamped into the jet electrodeposition equipment to start preparing the coating. The pH value of the plating solution was in the range of 1.0–1.5. The temperature of the plating solution was maintained at 60 °C by heating in a water bath. The gap between the nozzle and the surface of the workpiece during the jet electrodeposition process was 1.5 mm. The processing current density was in the range of 10–40 A/dm^2. After the coating was prepared, the workpiece was ultrasonically cleaned and dried.

Table 1. Composition of the plating solution

Plating solution compositions and operating conditions	Concentration (g/L)
$NiSO_4 \cdot 6H_2O$	120
$NiCl \cdot 6H_2O$	40
$FeSO_4 \cdot 7H_2O$	20
H_3PO_3	30
H_3BO_3	30
$C_6H_8O_7$ (Citric acid monohydrate)	10
CeO_2	1
CH_4N_2S (Thiocarbamide)	0.01
$C_{12}H_{25}SO_4Na$ (Sodium dodecyl sulfate)	0.08

2.2. Electrodeposition mechanism

Fig. 1 shows the schematic of the deposition mechanism whereby the Ni–Fe–P–CeO_2 composite is coated on a #45 steel substrate by jet electrodeposition, including four stages:

The first step involves crystal nucleation (Fig. 1a). Under the action of an external electric field, metal dissolution occurs at the anode, and a large number of metal ions is transferred to the cathode. Because of the strong adsorption of the nano-CeO_2 particles, some Ni^{2+}, Fe^{2+}, and PO_3^{2-} ions latch onto the nano-CeO_2 particles, forming aggregated particles.

The second step is characterized by the formation of nucleation sites (Fig. 1b). Some of the Ni^{2+}, Fe^{2+}, and P ions co-deposited in the solution form nucleation sites on the substrate surface.

The third stage is the grain growth stage (Fig. 1c). Under the action of an external electric field, Fe^{2+} and Ni^{2+} ions move to the cathode region, a reduction process occurs on the cathode substrate, the growth continues along the nucleation sites of the Ni and Fe grains, and the coating thickness increases.

In the fourth stage, the nano-CeO_2 particles are embedded on the coating surface (Fig. 1d). Nano-CeO_2 particles adsorbing Ni^{2+}, Fe^{2+}, and P are embedded on the coating surface and fill the surface defects on the coating.

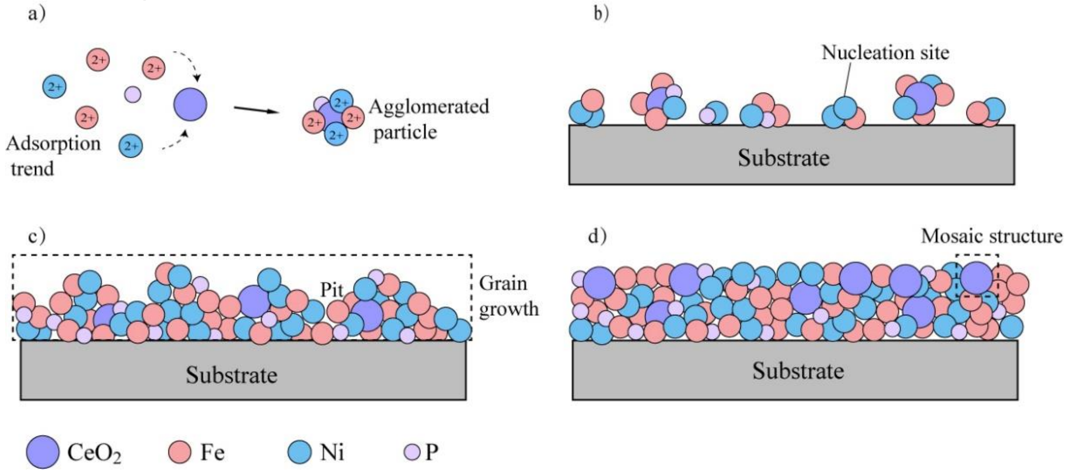

Figure 1. Schematic of the mechanism whereby the Ni–Fe–P–CeO_2 composite coating is formed

2.3. Sample characterization

A scanning electron microscope (FEI–SEM, Quanta FEG250; FE Instruments, Oregon, USA) was used to observe the surface morphology of the coating. An energy dispersive X-ray spectroscopy (EDS) spectrum analyzer (XFlash 5030 Bruker AXS, Inc., Berlin, Germany) was used to determine the chemical composition of the coating in the line scanning and plane scanning modes (1 mm^2). The phase structure of the coating was analyzed using an X-ray diffractometer (PANalytical X`pert; PANalytical Inc.) at an operating voltage of 40 kV, scan rate of 5 °/min, and scanning range of 20–90° to determine the phase structure. A microhardness measuring instrument (Duramin-40; Struers Inc., Denmark) was used to measure the microhardness of the composite coating surface. When testing, a GCr15 grinding ball with a diameter of 4 mm was selected, and the grinding ball was loaded onto the surface of the composite coating. The following parameters were set: Linear reciprocating friction for 20 min, reciprocating speed of 500 T/min, wear scar length of 4 mm, and test load of 320 g. Subsequently, five measurements were made, and the average value was taken as the measurement result. A wear test was carried out on a CFT-I material surface performance comprehensive tester. During the detection, the GCr15 grinding ball with a diameter of 4 mm was scratched back and forth on the coating surface for 20 min; the load was 320 g, and the scratch length was 4 m. An OLYMPUSLEXT4100 laser confocal microscope (Japan Olympus Company) was used to measure the dimensional parameters of the scratches on the coating surface. An electrochemical workstation (CS350; Wuhan Corrtest Instruments Corp., Ltd., China) was used to study the corrosion resistance of the composite coating. The test workpiece was immersed in a 3.5 wt.% NaCl solution, and a dynamic potential scan (a scan rate of 1 mV/s) method was applied to obtain the polarization curve of the coating. Subsequently, the epitaxy method was applied to obtain the parameters that characterize the corrosion resistance-self-corrosion potential and self-corrosion current. The AC impedance method (EIS) was used to measure the impedance spectrum of the coating in the corrosive medium at the open circuit potential. The test frequency range was 10^{-2}–10^{-5} Hz, swept from high frequency to low frequency. The ZSimpWin software was used to fit and analyze the obtained impedance spectrum.

3. RESULTS AND DISCUSSION

3.1. Surface morphology

Fig. 2 shows the surface morphologies of the composite coatings prepared under different current densities, obtained by FEI–SEM. In the process of jet electrodeposition, the catalytic active center on the substrate surface induces a co-deposition of Ni, Fe, P, and CeO_2, and its growth rule follows a 2D crystal growth model. Thus, a cell structure is gradually formed. At low current densities (Fig. 2a), there are more irregular depressions and protrusions on the coating surface, accompanied by cracks and particle adhesion, and the coating surface is relatively rough. This is because at low current densities, the transfer rate of metal ions to the cathode is low, and the hydrogen gas precipitated near the cathode cannot be eliminated in time, hindering the deposition of metal ions on the coating surface. Moreover, the number of nucleation sites on the coating surface is reduced, and the nucleation rate is low, resulting in a thin coating and a low surface density. When the current density increases to 20 A/dm^2 (Fig. 2b), the surface morphology of the coating is improved, the number of protrusions is reduced, and the grain boundary structure becomes a flat-cell structure; however, the surface contains “sheet-like” substances and adhered particles. Based on the atomic content ratio obtained from the EDS, the “flaky” substances represent the oxides of Fe and Ni. This is due to the increase in the current density, enhancement in the hydrogen evolution reaction (HER) [26], and weakening of the deposition process of metal ions, which is conducive to the rise in impurities. The growth of Ni, Fe, P, and CeO_2 grains during the co-deposition process is accelerated; however, the current efficiency is low, and therefore, the ions easily form oxide deposits on the coating surface.

When the current density is 30 A/dm^2 (Fig. 2c), the area of the cell structure of the coating increases and is evenly distributed. The boundary of the cell structure is blurred, there is no evident protrusion, and there are fewer attached particles. This shows that the coating structure is compact and dense. This is because the increased current density and current efficiency led to a decrease in the surface energy of the nano-CeO_2 particles, thus decelerating their agglomeration process [27]. Because of the adsorption of the cathode surface potential, the nano-CeO_2 particles in the plating solution can be evenly distributed on the surface of the plating layer, the nucleation sites of Ni and Fe grains are increased, the grains are refined [28], the cell structure is compact, and the density is high. When the current density continues to increase to 40 A/dm^2 (Fig. 2d), the cathode potential is too high, the ion deposition rate is too high, the coating thickness increases, and the stress on the surface of the coating is too concentrated causing the coating to crack. This is because the current density is too high, the transfer of metal ions to the cathode is accelerated, and the grains grow on the coating surface, resulting in excessive stress on the surface concentration increases the brittleness of the coating, and cracks appear on the surface of the composite coating under uneven stress. The excessive current density increases the surface energy of the nano-CeO_2 particles, making them to absorb more charge, the agglomeration phenomenon of mutual adsorption is strengthened, and the surface roughness of the coating increases. Therefore, an excessive current density is not conducive to improving the chemical properties of the coating.

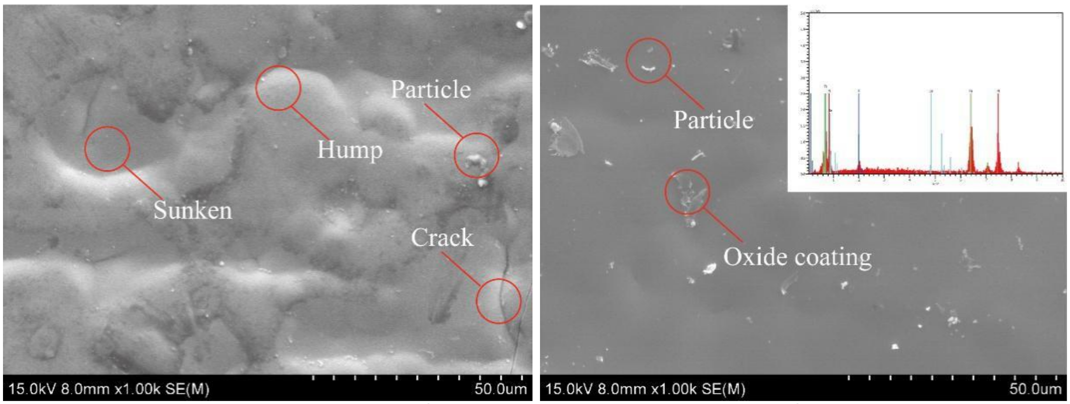

(a) 10 A/dm^2 (b) 20 A/dm^2

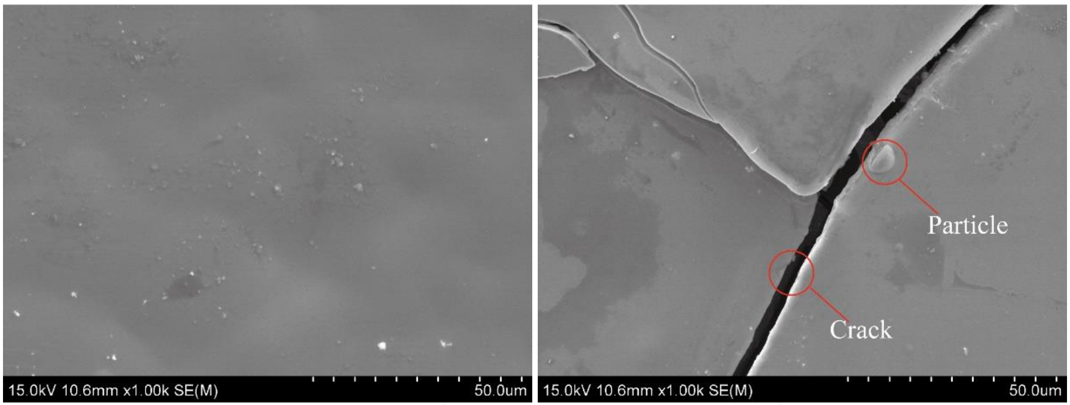

(c) 30 A/dm^2 (d) 40 A/dm^2

Figure 2. Surface morphology of Ni–Fe–P–CeO_2 composite coatings prepared under varying current density

3.2. XRD and EDS analyses

Fig. 3 shows the X-ray diffractometry (XRD) pattern of the Ni–Fe–P–CeO_2 composite coating prepared under different current densities. The composite coating has an amorphous structure; with the increase in the current density, the phase structure of the coating changes from nanocrystalline to amorphous. When the current density is too high, nanocrystalline characteristics once again appear [29]. Since P is co-deposited with metals Fe and Ni to form a solid solution, the content of nano-CeO_2 particles in the plating solution is low, and their respective characteristic peaks are not detected in the XRD pattern. At a current density of 10 A/dm^2, the characteristic composite peaks of Fe(110) and Ni(111) can be seen at approximately $2\theta = 45°$. Moreover, there are weak peaks of Fe(211) and Ni(200), which belong to the face-centered cubic (FCC) lattice. This confirms the successful preparation of the Ni–Fe–P–CeO_2 composite coating; when the current density reaches 20 A/dm^2, the broadening of the characteristic peaks of Fe(110) and Ni(111) is evident, and the difference in strength is reduced. Moreover, because of the increase in the current density, the grains continue to grow, and the crystal phase content increases. When the current density is 30 A/dm^2, the characteristic peak of FeNi(111) exhibits a “steamed bun” shape. The characteristic weak peaks of Fe(110) and Ni(111) gradually disappear. The composite coating layer changes from a crystal structure to an amorphous one. The increase in the current density increases the nucleation rate of the crystal grains on the coating layer surface. The grains are refined, and a stable FeNi phase is formed on the surface, while the current density continues to increase to 40 A/dm^2. The main peak is (Ni, Fe)(111) with $2\theta = 43.917°$, attributed to the eutectic reaction that occurred during the abnormal deposition of Fe^{2+} and Ni^{2+} under an excessive current density, forming an (Ni, Fe) intermetallic compound phase. In addition, the atomic radius of the nano-CeO_2 particles as a rare earth element is larger than that of the transition zone metal. When nano-CeO_2 particles are solid-dissolved in a matrix material, the residual stress in the coating layer increases, inducing a lattice distortion of the metal atoms. The existence of residual stress causes the grain orientation to shift, and the grains grow epitaxially in the preferred orientation, which explains the shift in the Fe(110) characteristic peak to the left in the XRD pattern.

Table 2 lists the percentage change in the atomic content of each element in the coating under different current densities. As the current density increases, the Fe content increases first and then decreases; the Ni content decreases first and then increases; the P element content shows no significant change; and the Ce content increases from 1.07 at.% to 1.98 at.%. When the current density is 10 A/dm^2, the Fe and Ni contents are 47.96 and 46.89 at.%, respectively. When the current density is 20 A/dm^2, the Fe content increases to 51.11 at.%, whereas the Ni content decreases to 41.63 at.%. When the current density is 30 A/dm^2, the maximum Fe content in the composite coating reaches 51.64 at.%, and the Ni content increases to 42.91 at.%. When the current density is 40 A/dm^2, the Fe content in the composite coating decreases to 41.53 at.%, and the Ni content increases to 50.57 at.%. This is because Fe^{2+} inhibits the reduction process of Ni^{2+}. An increase in the current density accelerates the transfer rate of metal ions to the cathode. Fe^{2+} forms $Fe(OH)_2$ near the cathode, inhibiting the reduction of Ni^{2+}, resulting in Ni in the coating. The element content decreases, whereas the Fe content increases. With increasing current density, the dispersion of the nano-CeO_2 particles is strengthened. Because of its strong adsorption on the surface, the surface-active particles compete with $Fe(OH)_2$ to suppress the precipitation of Fe elements, while the deposition of Ni^{2+} ions is suppressed, and Ni^{2+} is reduced. The substrate surface is deposited and co-deposited with P to form a solid solution. This increases the Ni content in the plating layer and decreases the Fe content. Therefore, increasing the current density is beneficial to increasing the Ni content in the plating layer.

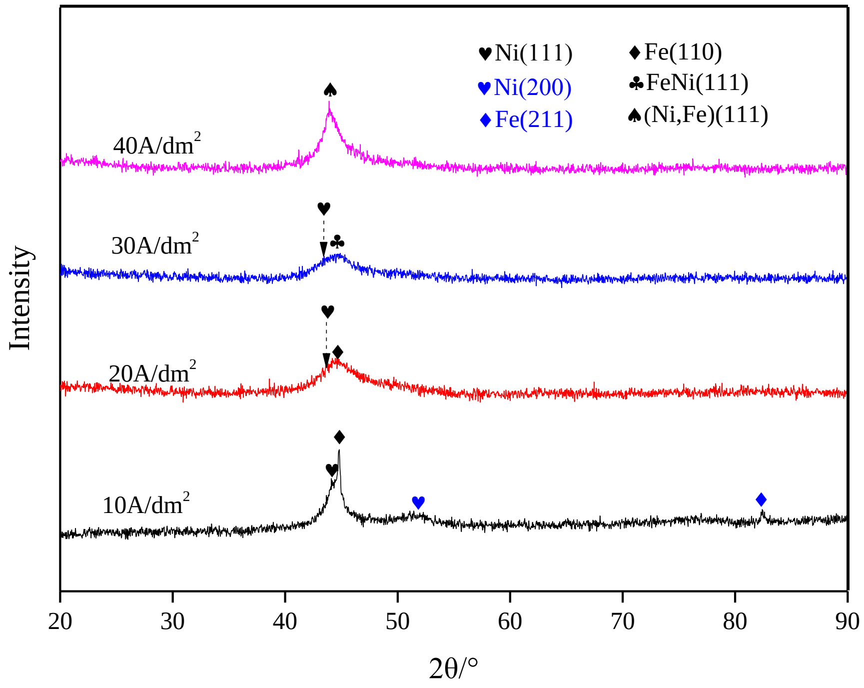

Figure 3. XRD spectra of Ni–Fe–P–CeO_2 composite coatings as a function of the current density

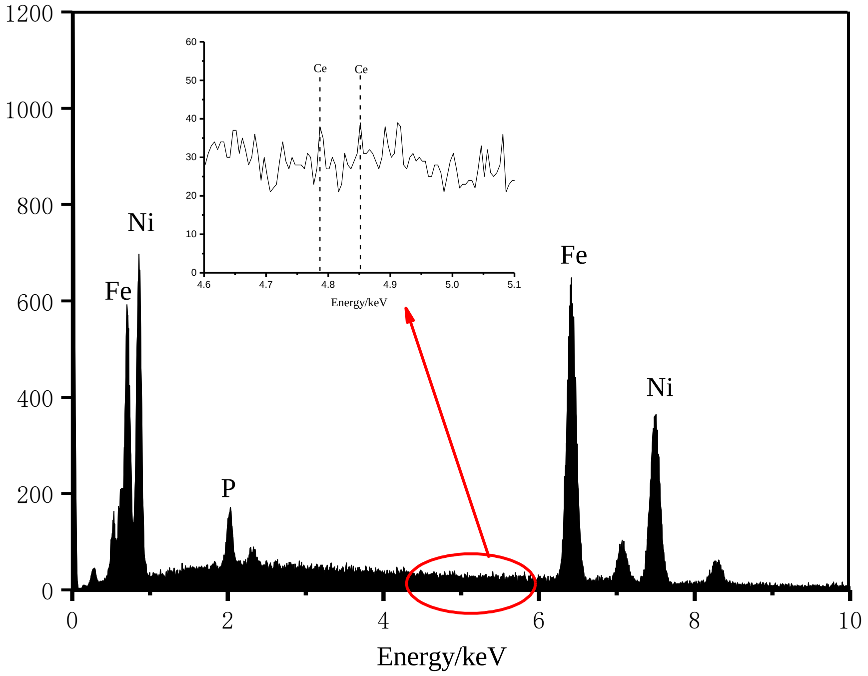

Figure 4. Energy dispersive spectroscopy (EDS) analysis of Ni–Fe–P–CeO_2 composite coating

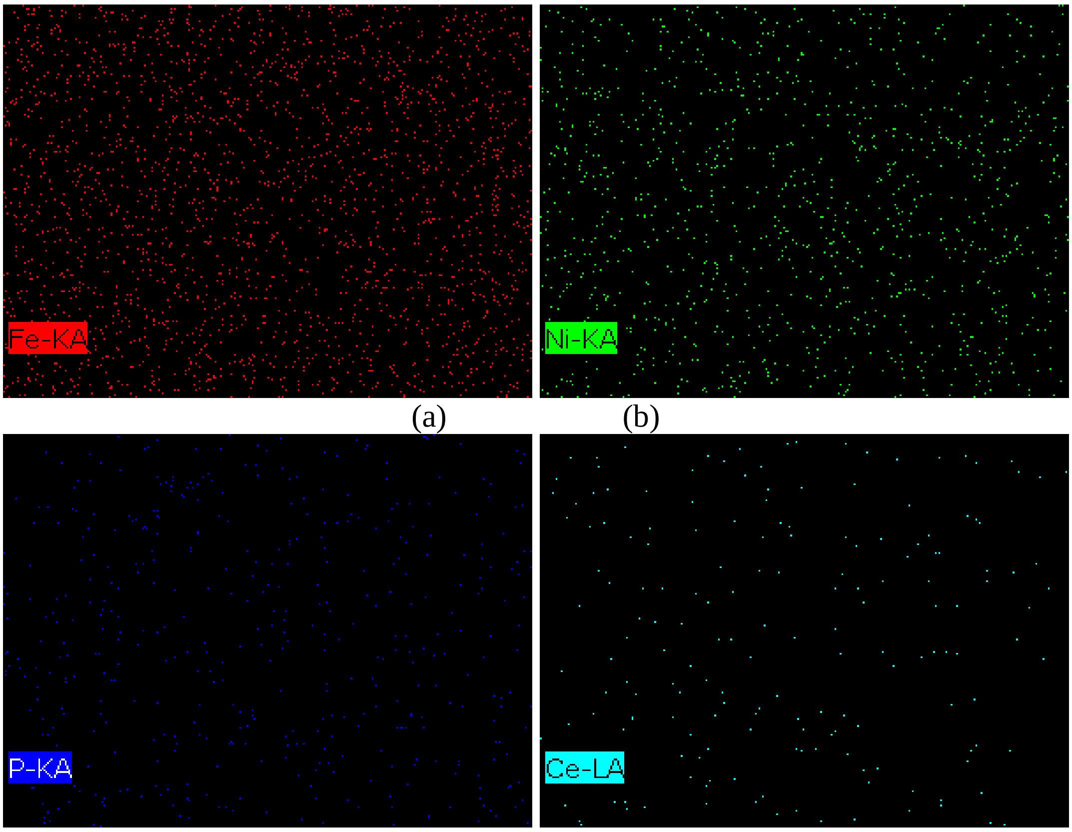

(a) (b)

(c) (d)

Figure 5. Distribution diagram of Ni–Fe–P–CeO_2 elements at a current density of 30 A/dm^2: (a) Fe; (b) Ni; (c) P; (d) Ce

Fig. 4 shows the EDS surface scanning result of the coating surface when the current density is 30 A/dm^2. The coating mainly contains Fe and Ni, followed by P and lastly Ce. CeO_2 only plays a role of strengthening phase in the plating solution. Fig. 5 shows the distribution of the elements on the composite coating surface when the current density is 30 A/dm^2. When the current density is 30 A/dm^2, the elements on the coating surface are evenly distributed, and there is no evident agglomeration of the nano-CeO_2 particles. This shows that a current density of 30 A/dm^2 in the electroplating process is conducive to the uniform distribution of the elements and particles in the coating. A related research showed that the uniformity of the particle distribution on the coating surface influences the wear and corrosion resistances of the coating [30].

Table 2. Elemental chemical composition (at. %) of Ni–Fe–P–CeO_2 composite coating obtained by EDS

	10 A/dm^2	20 A/dm^2	30 A/dm^2	40 A/dm^2
Fe (at.%)	47.96	51.11	51.64	41.53
Ni (at.%)	46.89	41.63	42.91	50.57
P (at.%)	4.08	5.70	4.08	5.93
Ce (at.%)	1.07	1.56	1.37	1.98

3.3. Microhardness

Fig. 6 shows the microhardness of the composite coatings prepared under different current densities. With the increase in the current density, the microhardness of the composite coating tends to increase first and then decrease, consistent with previous results [31]. The average microhardness value of 313.59 $HV_{0.1}$ indicates that at low current densities, the particles in the coating are unevenly distributed, the grain growth rate is low, and the coating is thin, thus decreasing the microhardness of the composite coating. When the current density is 20 A/dm^2, the average microhardness of the composite coating is increased to 540.98 $HV_{0.1}$, the increase in cathode potential improves the agglomeration of the nano-CeO_2 particles, the ion deposition rate is accelerated, the coating thickness is increased, and the microhardness is promoted. When the current density is 30 A/dm^2, the average microhardness of the composite coating reaches a maximum value of 614.24 $HV_{0.1}$, which is 95.81% higher than that of the Ni–Fe–P–CeO_2 alloy coating at a current density of 10 A/dm^2. This is because increasing the current density makes the grain refinement and dispersion stronger. The CeO_2 nanoparticles dispersed in the plating solution segregate at the crystal interface with tiny solid particles and hinder the growth of the cell structure; moreover, the rare earth oxide segregated at the boundary also forms a rare earth compound phase with the impurity atoms at the boundary. The new phase plays a pinning role, strengthens the alloy by hindering the movement of the dislocations and stabilizing the dislocation substructure, while forming a compound with a high melting point, high hardness, and high dispersion with the other elements in the Ni-based coating, thereby substantially improving the strength and hardness of the alloy. However, when the current density continues to increase to 40 A/dm^2, the average microhardness of the composite coating is 478.53 $HV_{0.1}$, indicating that the current density is too high and is not conducive to the uniform distribution of the nano-CeO_2 particles, Fe^{2+}, and Ni^{2+}. The surface deposition is uneven, and the microhardness of the coating tends to decrease.

Therefore, increasing the processing current density can help improve the microhardness of the composite coating surface [32]. When the current density increases to 30 A/dm^2, the microhardness value of the composite coating is maximum. At too high current densities, the internal stress of the coating surface is too high, which is not conducive to the microhardness of the composite coating.

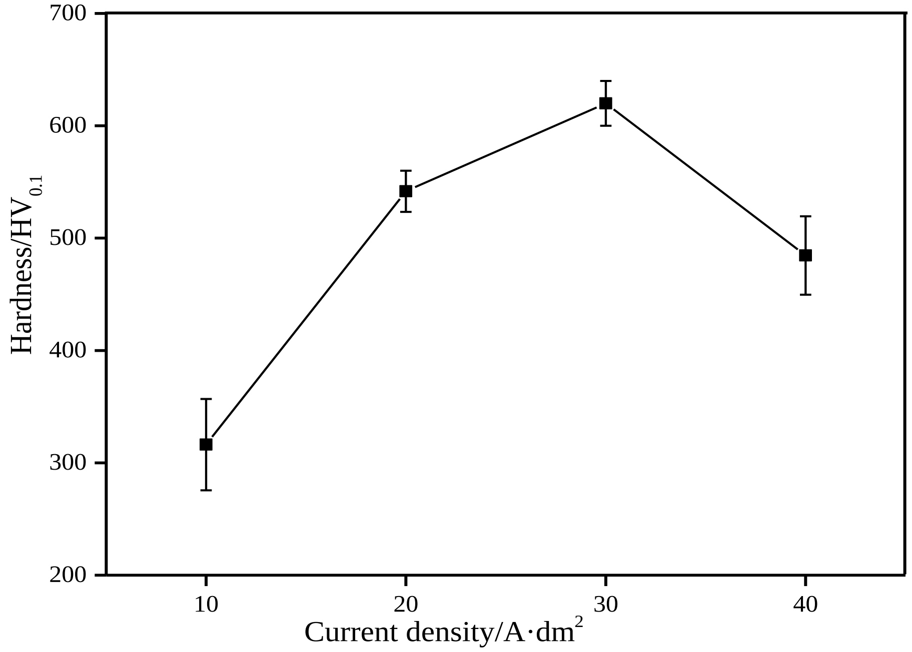

Figure 6. Microhardness of Ni–Fe–P–CeO_2 composite

3.4. Wear resistance

Fig. 7 shows a schematic of the micro-morphology of the coating layer after friction and wear under the same wear conditions. Studies have shown that the microhardness of a coating has a direct effect on the wear resistance of the coating. The higher the microhardness of the composite coating, the better its wear resistance [33]. The coating shown in Fig. 7a is the most severely worn, with several peeling marks and cracks on the surface of the wear scar. Ploughs can be observed in parallel around the edges of the wear scar. Because of the low hardness and thin coating produced at low current densities, the adhesive node is prone to shear fracture. After the coating is sheared, it forms abrasive debris and migrates from one surface to another surface, causing serious adhesive wear. According to the strength theory, the greater the plastic deformation, the more severe the adhesion and wear of the coating [34]. Under the cyclic effect of contact stress, the Ni–Fe–P–CeO_2 composite coating exhibits surface fatigue because of the excessive plastic deformation on the surface, which destroys the supporting load-bearing capacity of the coating. Cracks begin to appear at the stress concentration areas on the coating surface, which then undergoes an internal expansion, eventually resulting in fatigue wear and flaking.

Fig. 7b shows significant peeling off at the wear interface. A furrow appears at the middle of the wear scar, accompanied by a small amount of abrasive wear. As the current density increases, the autoenergy of the nano-CeO_2 particles increases, the surface energy decreases, the adsorption capacity of the surrounding nano-CeO_2 particles decreases, the agglomeration phenomenon decreases, the number of nucleation sites and nucleation rate increase, and the crystal grains become finer. To make the Ni–Fe–P–CeO_2 distribution in the composite coating more uniform, the nano-CeO_2 particles play a bearing role in the relative sliding process of the coating and the friction pair, suppress the expansion of the adhesion area of the friction surface, and wear off, and the anti-contact of the coating. Thus, the wear ability is improved [35].

Gray-black abrasive debris can be observed at the wear interface shown in Fig. 7c. This indicates that the surface of the composite coating has a high hardness and good wear resistance. Owing to the special 4F structure of the rare-earth element CeO_2 [36], it has a strong chemical activity and a low melting point. It can act as a lubricant during the relative sliding of the friction pair. An appropriate number of nano-CeO_2 particles can avoid the expansion of the contact stress on the coating surface to the inner layer, thereby decreasing the shearing between the friction contact surfaces and the degree of wear of the coating surface. Abrasive wear and oxidative wear are the main forms of wear. The coating surface is protected, and the corrosion resistance is significantly improved.

The coating on the surface is slightly peeled off, as shown in Fig. 7d. There are cracks around this region and a clear furrow at the center of the wear scar, accompanied by wear and adhesion. When the current density is too high, the coating thickness increases, and the hardness decreases. In addition, the nano-CeO_2 particles have a high hardness, and the unevenly distributed nano-CeO_2 particles in the coating easily detach when worn. They adhere to the surface of the coating and move relative to the friction pair, forming a "microscopic cutting action," which increases the wear of the coating and decreases the wear resistance of the composite coating [37].

Combined with the analysis results of the EDS spectrometer line scan, shown in Fig. 7, the characteristics of the Fe–Ni content curve, shown in Fig. 7e, are explained as follows. The Fe content sharply increases at the coating wear point, whereas the Ni content sharply decreases. This is because of the following reasons: the plating layer prepared at low current densities is suppressed due to the ion deposition rate, the plating layer is thin and worn out during wear, the microhardness is low, a large amount of increased Fe comes from the base workpiece, and the base material does not contain Ni. In Fig. 7f, the Fe and Ni contents still exhibit large fluctuations. The atomic percentage of Fe increases, whereas that of Ni decreases, indicating that the wear scar interface contains fewer plating wear-through points. In Fig. 7g, the element atomic percentage contents of Fe and Ni vary smoothly, indicating that the plating layer is less damaged during friction and wear and that the coating has excellent corrosion resistance. In the line scan shown in Fig. 7h, the atomic percentage content curves of Fe and Ni elements fluctuate. In the central area of wear, the atomic percentage content of Fe increases, whereas that of Ni increases first and then decreases. This shows that after the coating surface is abraded, the coating layer is oxidized and abraded. Therefore, the plating layer prepared at a current density of 30 A/dm^2 exhibits the least fluctuation in the atomic percentage contents of Fe and Ni, and this coating has the best wear resistance.

As shown in Fig. 8 and Table 3, as the current density increases, the width, depth, and cross-sectional area of the wear scar decrease first and then increase. When the current density is 10 A/dm^2, the wear scar width of the composite coating is 813 μm, the wear scar depth is 21 μm, and the cross-sectional area is 14348 μm^2. When the current density is increased to 20 A/dm^2, the width of the wear scar of the composite coating is reduced to 802 μm, the depth of the wear scar is reduced to 18 μm, and the cross-sectional area is reduced to 10740 μm^2. When the current density is 30 A/dm^2, the width, depth, and cross-sectional area of the wear scar are the lowest: 732 μm, 13 μm, and 8584 μm^2 respectively. Compared with the composite coating prepared at a current density of 10 A/dm^2, the wear scar width, scar depth, and cross-sectional area are reduced by 9.88, 37.34, and 40.17%, respectively. Under the same wear conditions, the wear scars have the same length, and the smallest cross-sectional area corresponds to the best wear resistance. When the current density continues to increase to 40 A/dm^2, the parameters of the wear scar interface start exhibiting an upward trend. The wear scar width, wear scar depth, and cross-sectional area increase to 768 μm, 14 μm, and 9076 μm^2, respectively. Therefore, at a current density of 30 A/dm^2, because of the enhancement in the fine grain strengthening, dispersion strengthening, and pinning strengthening of the coating, the coating exhibits the highest hardness and the best wear resistance.

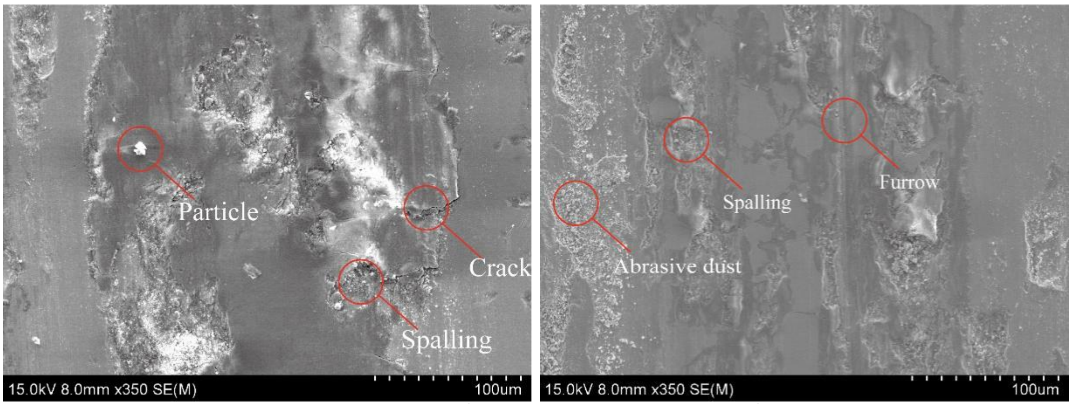

(a) 10 A/dm^2 (b) 20 A/dm^2

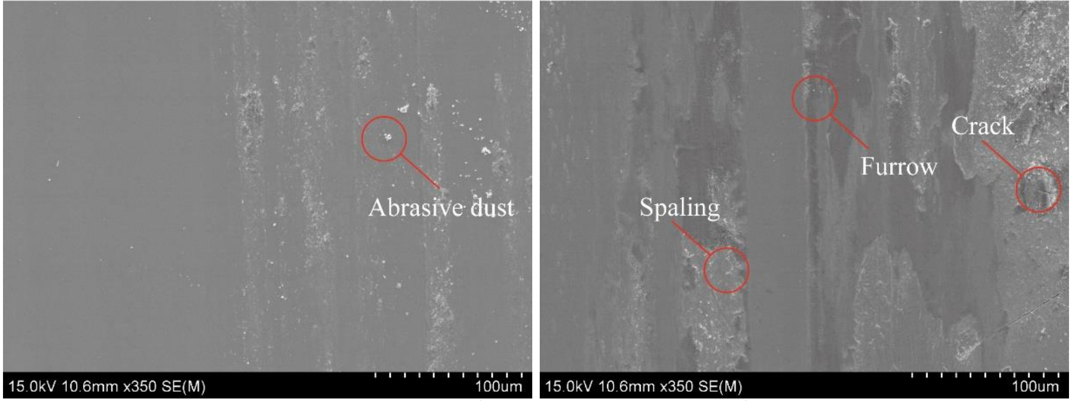

(c) 30 A/dm^2 (d) 40 A/dm^2

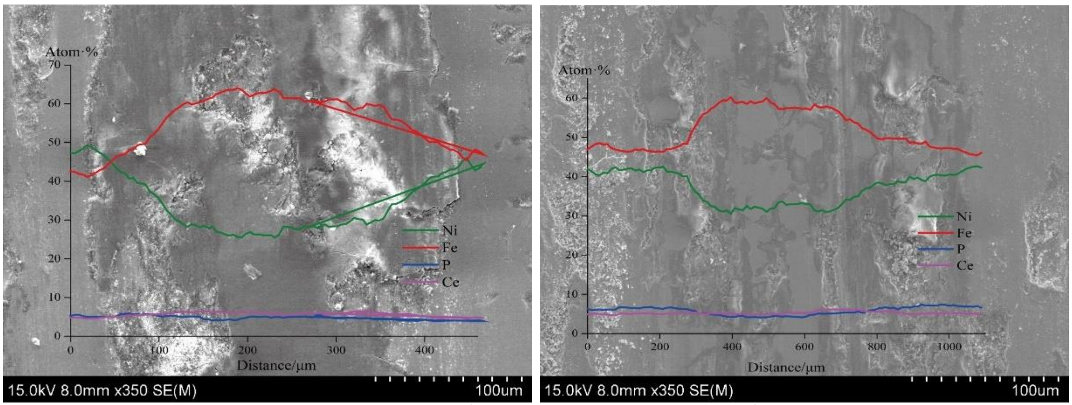

(e) 10 A/dm^2 (f) 20 A/dm^2

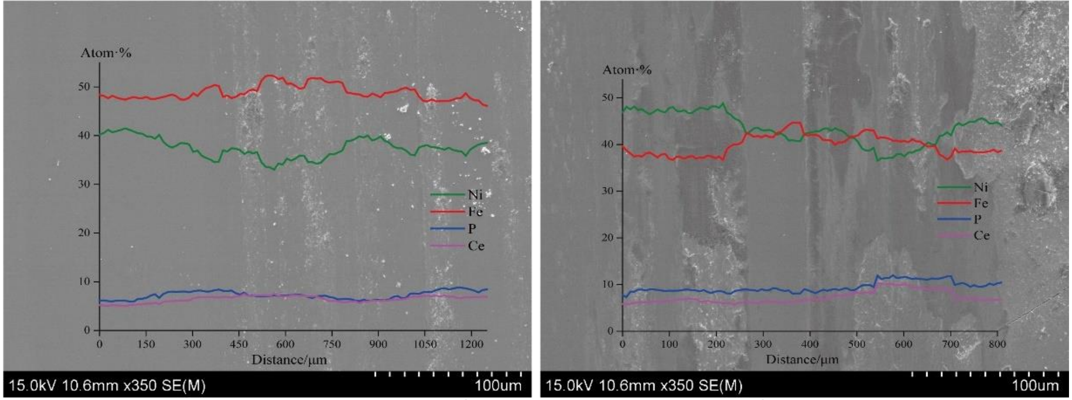

(g) 30 A/dm^2 (h) 40 A/dm^2

Figure 7. Surface morphology of wear marks

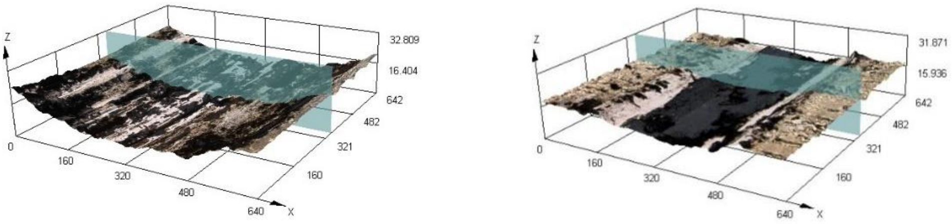

(a) 10 A/dm^2 (b) 20 A/dm^2

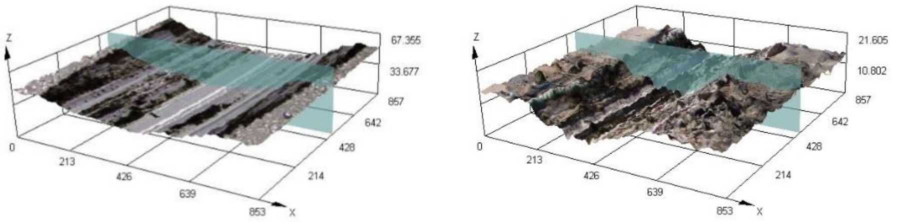

(c) 30 A/dm^2 (d) 40 A/dm^2

Figure 8. Outlines of wear interface at various current densities

Table 3. Parameters of wear mark section

Current density (A/dm^2)	Width (μm)	Height (μm)	Scratch (μm^2)
10	813	21	14348
20	802	18	10740
30	732	13	8584
40	768	14	9076

3.5. Corrosion resistance analysis of Ni–Fe–P–CeO$_2$ composite coatings

3.5.1. Potentiodynamic polarization curve

The self-corrosion potential and self-corrosion current can reflect the corrosion resistance of a composite coating. Generally, the lower the self-corrosion current density of a composite coating, the lower the corrosion rate; the greater the self-corrosion potential, the more difficult it is for the corrosion process to occur, and the better the corrosion resistance of the coating [38,39]. Table 4 lists the corrosion potential, corrosion current, and corrosion rate, calculated using the *CorrTest* software and the polarization curve epitaxy method. Here, B_a and B_c are the anode and cathode dynamic potential polarization slopes, respectively. As shown in Fig. 9 and Table 4, with the increase in the current density applied to prepare the Ni–Fe–P–CeO$_2$ compound coating, the self-corrosion potential increases first and then decreases, whereas the self-corrosion current density and corrosion rate tend to decrease first and then increase. At a current density of 10 A/dm^2, the self-corrosion voltage of the composite coating is −0.756 V, and the self-corrosion current is 1.062×10^{-5} A·cm^{-2}, indicating that the coating has a low corrosion resistance. When the current density increases to 20 A/dm^2, the self-corrosion voltage of the composite coating is −0.619 V, the self-corrosion current is 8.160×10^{-6} A·cm^{-2}, and the corrosion resistance of the coating is improved. When the current density is 30 A/dm^2, the self-corrosion potential reaches the maximum value of −0.359V, and the self-corrosion current density reaches the minimum value of 3.480×10^{-6} A·cm^{-2}. At this time, the corrosion rate is at least 0.042 mm/a, and the corrosion resistance of the coating layer is the best. When the current density continues to increase to 40 A/dm^2, the corrosion potential shifts negatively. At this time, $E_{corr} = -0.602$V, $I_{corr} = 3.684\times10^{-5}$ A·cm^{-2}, the corrosion rate is increased to 0.446 mm/a, and the corrosion resistance of the coating decreases.

The results of the potentiodynamic polarization curve and corrosion parameter analysis show that the composite coating prepared at a current density of 30 A/dm^2 exhibits the highest self-corrosion potential, the lowest self-corrosion current and corrosion rate, and the best corrosion resistance.

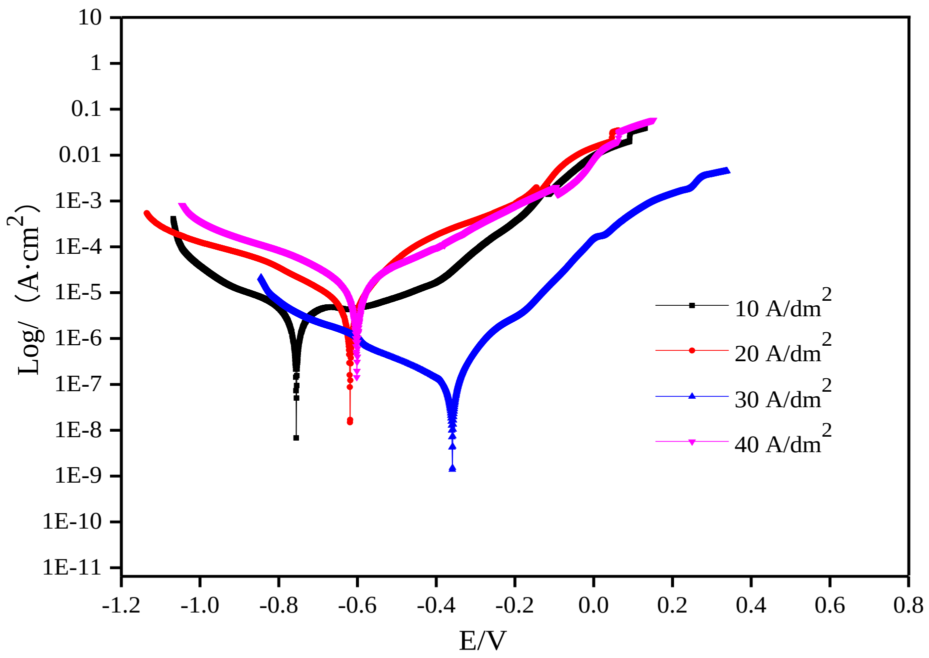

Figure 9. Potentiodynamic polarization curve of Ni–Fe–P–CeO_2 composite coating prepared by jet electrodeposition

Table 4. Corrosion electrochemical parameters of Ni–Fe–P–CeO_2 composite coatings prepared by jet electrodeposition

Current density (A/dm^2)	B_a (mV/dec)	B_c (mV/dec)	I_{corr} (A·cm^{-2})	E_{corr} (V)	Corrosion rate (mm/a)
10	143	370	1.062×10^{-5}	−0.756	0.129
20	175	303	8.160×10^{-6}	−0.619	0.099
30	427	264	3.480×10^{-6}	−0.359	0.042
40	376	311	3.684×10^{-5}	−0.602	0.446

3.5.2. EIS diagram

The corrosion behavior of the Ni–Fe–P–CeO_2 composite coatings with an open circuit potential in a 3.5% NaCl solution was investigated by EIS. Fig. 10 shows the Nyquist diagram obtained from the AC impedance test of the coating at different scanning frequencies. Table 5 lists the parameter values obtained after fitting the equivalent circuit model shown in Fig. 11, where R_s is the resistance of the corrosion solution, R_p is the charge transfer resistance, CPE is the constant phase angle element, and the impedance is

$$Z = \frac{1}{Y_0(j\omega)^{-n}}$$

Where the constant Y_0 has a dimension of $\Omega^{-1}\cdot cm^{-2}\cdot s^{-n}$, and the parameter n is a dimensionless index. If n = 0, the CPE element is a pure resistor; if n = 1, the CPE element is an ideal capacitor. In practical applications, the value of n ranges from 0 to 1 [40]. The radius of the capacitive impedance arc is related to the charge transfer resistance. The greater the radius of the capacitive impedance arc, the greater the value of the charge transfer resistance and the lower the corrosion rate [41].

Fig. 10 shows the change rule of the capacitance arc resistance corresponding to the composite coating prepared under different current densities; the resistance first increases and then decreases. The magnitude of the capacitance impedance arc of the Ni–Fe–P–CeO_2 composite coatings prepared under different current densities is in the following order (in terms of the current density): 30 A/dm^2 > 20 A/dm^2 > 40 A/dm^2 > 10 A/dm^2. When the current density is 10 A/dm^2, the capacitance impedance arc radius is the smallest, and the charge transfer resistance of the composite coating is only 649 $\Omega\cdot cm^{-2}$. At this time, the corrosion resistance of the coating is the worst. When the current density increases to 20 A/dm^2, the arc radius of the capacitance impedance increases, the charge transfer resistance of the composite coating increases to 1535 $\Omega\cdot cm^{-2}$, and the corrosion resistance of the coating improves. When the current density is 30 A/dm^2, the corresponding capacitance impedance arc size is the largest, and the charge transfer resistance is 6891 $\Omega\cdot cm^{-2}$. When the current density continues to increase to 40 A/dm^2, the arc radius of the capacitor impedance decreases, the charge transfer resistance decreases to 445.7 $\Omega\cdot cm^{-2}$, and the corrosion resistance of the coating decreases. This is consistent with the results of the potentiodynamic polarization curve.

In summary, a change in the current density affects the distribution of the nano-CeO_2 particles on the surface of the coating. Uniformly distributed nano-CeO_2 particles promote the density of the coating surface and the corrosion resistance of the coating.

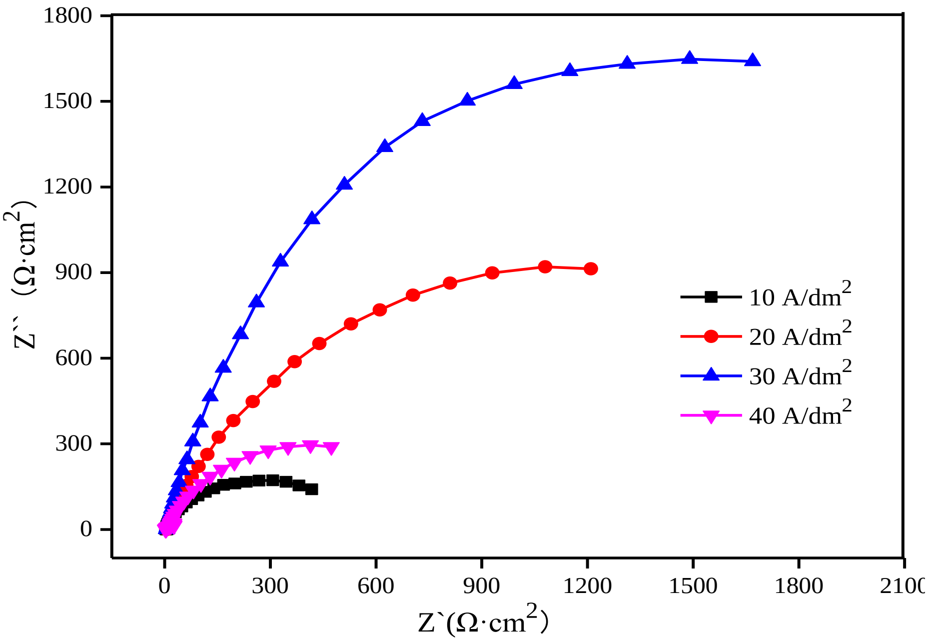

Figure 10. Nyquist diagram of coatings prepared under different current densities

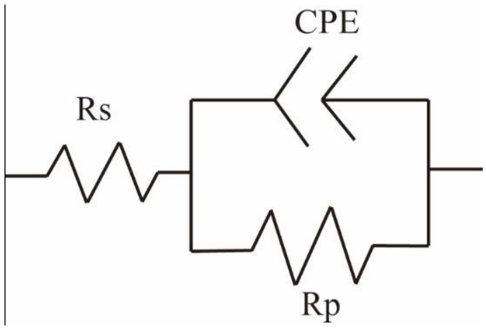

Figure 11. Equivalent electrical circuits CPE model

Table 5. Fitted corrosion parameters for Ni–Fe–P–CeO_2 composite coatings

	10 A/dm^2	20 A/dm^2	30 A/dm^2	40 A/dm^2
R_S ($\Omega\cdot cm^{-2}$)	2.665	5.857	5.838	6.333
CPE-T	0.0084785	0.015697	0.0046197	0.0081981
CPE-P	0.50882	0.86648	0.8819	0.84136
R_P ($\Omega\cdot cm^{-2}$)	649	1535	6891	445.7

3.5.3. Corrosion morphology and mechanism

Fig. 12 shows the surface morphology obtained by FEI–SEM after the workpieces prepared at various current densities are placed in a 3.5% NaCl solution and subjected to a corrosion treatment for 2 h. The surface morphology of the coating prepared at a current density of 10 A/dm^2 (Fig. 12a) is the worst, the coating is severely eroded, many corrosion pits are formed on the coating surface, and there are wide gaps and depressions in the corrosion pits. The protection mechanism of the coating on the substrate is invalid. When the current density is 20 A/dm^2 (Fig. 12b), the corrosion interface of the prepared coating exhibits surface shedding, accompanied by cracks, and the corrosion situation is improved. The surface of the coating (Fig. 12c) prepared at a current density of 30 A/dm^2 is slightly corroded. After being corroded, the surface of the coating is peeled off to form a “gully,” with fewer cracks and particles (corrosion products) attached. When the current density is increased to 40 A/dm^2 (Fig. 12d), the corrosion is aggravated, with pits of varying depths, and multiple corrosion pits on the surface of the overlapping layer. The composite coating prepared at a current density of 30 A/dm^2 has the best corrosion resistance, consistent with the results of the potentiodynamic polarization curve.

From the analysis made in Section 3.1, the surface of the composite coating prepared at low current densities is uneven and has a high roughness (low smoothness), which promotes the formation of corrosion sites of Cl^- ions, with pitting corrosion being the main corrosion mechanism. The current density continues to increase, which is conducive to improving the density of the surface morphology of the coating. At 30 A/dm^2, the cell structure on the coating surface is compact, and the density is the best. However, the surface smoothness of the Ni–Fe–P–CeO_2 composite coating at 40 A/dm^2 is slightly lower than that at 30 A/dm^2, making it easier to form more corrosion sites on the coating surface, and the corrosion resistance of the coating is reduced.

Fig. 13 shows a schematic of the corrosion protection mechanism whereby the Ni–Fe–P–CeO_2 composite is coated on the substrate in a 3.5 wt% NaCl solution. The surface morphology of the coating layer affects the corrosion resistance of the coating, and improves the flatness and compactness of the coating layer, thereby improving the corrosion resistance of the coating layer. The composite coating prepared at low current densities (Fig. 13a) exhibits a low surface smoothness and microdefects. Cl^- ions in the corrosion solution are likely to form several corrosion sites near the defects, causing severe local corrosion and localized coatings. Shedding, the substrate is directly exposed to the corrosive solution, the coating layer loses protection to the substrate, and eventually causes the parts to fail [42]. The current density gradually increases (Fig. 13b), the agglomeration of the nano-CeO_2 particles in the coating is weakened, the coating distribution is uniform, the grains are refined, the surface smoothness is the best, and the Cl^- ions are suppressed. The formation of corrosion sites on the surface of the coating layer, along with the nano-CeO_2 particles, lead to gaps, holes, and other structural defects during the jet electrodeposition process, forming a corrosion primary cell with the coating layer, which improves local corrosion and pitting corrosion. Increasing the current density is conducive to the formation of Fe and Ni oxides (NiO, Fe_2O_3, etc.), combined with corrosion products to form a passivation film on the coating surface [43,44]. It effectively prevents the formation and diffusion of corrosion sites. Pitting corrosion is transformed into uniform corrosion, and the #45 steel substrate is effectively protected against corrosion.

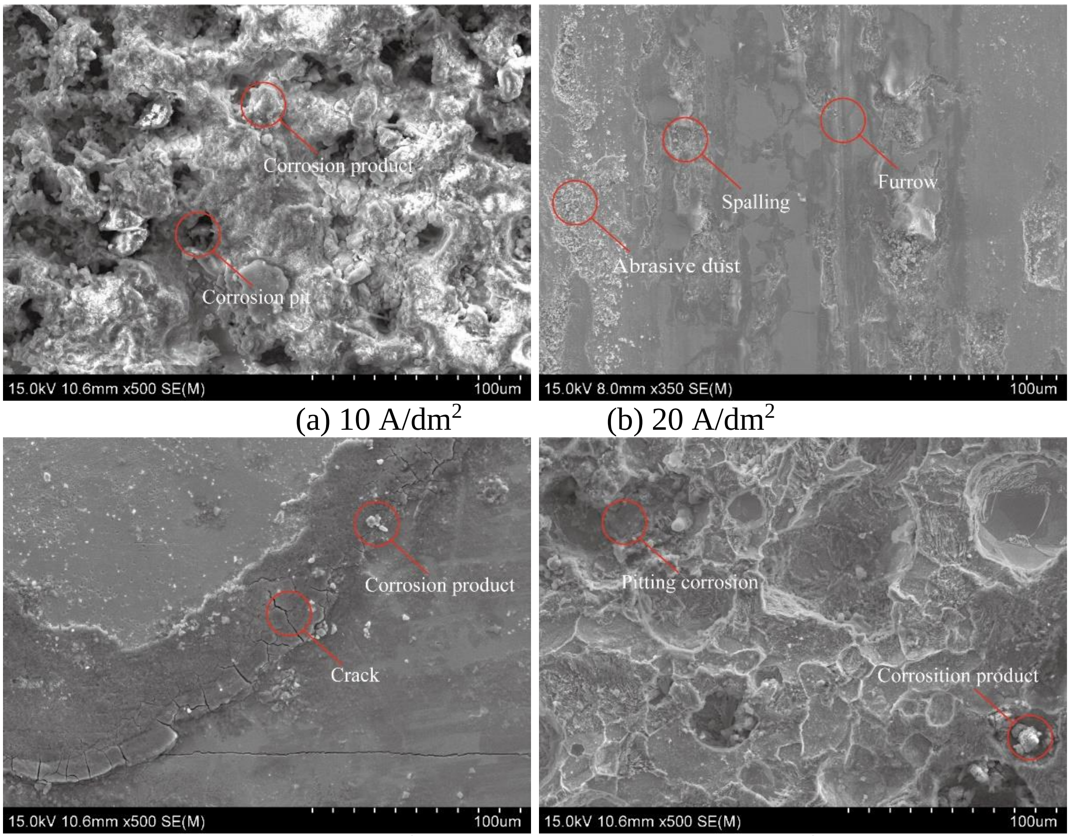

(a) 10 A/dm^2 (b) 20 A/dm^2

(c) 30 A/dm^2 (d) 40 A/dm^2

Figure 12. Microstructures of corroded Ni–Fe–P–CeO_2 composite coatings prepared at current densities of: (a) 10 A/dm^2; (b) 20 A/dm^2; (c) 30 A/dm^2; (d) 40 A/dm^2

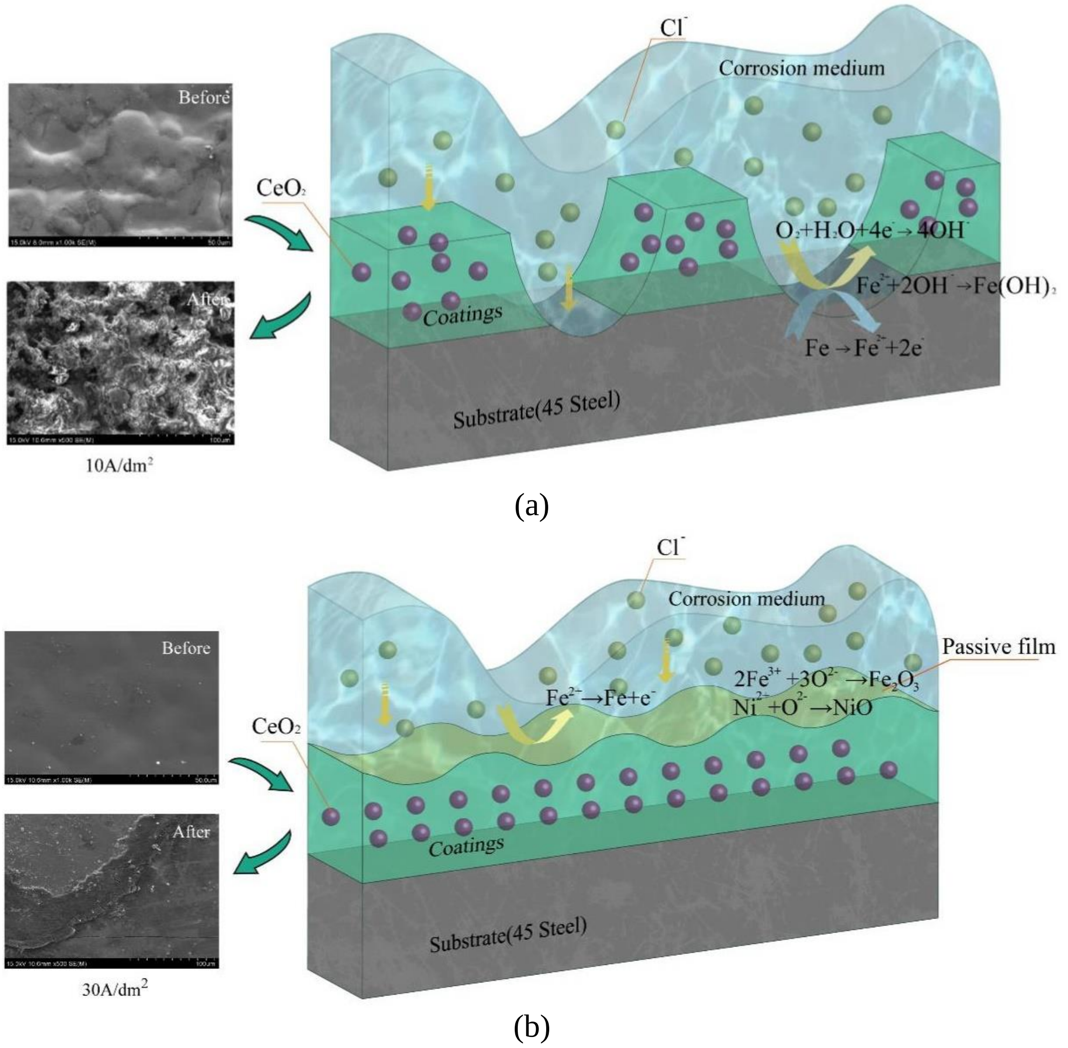

Figure 13. Corrosion resistance mechanism of Ni–Fe–P–CeO$_2$ composite coatings in a 3.5 wt% NaCl solution: (a) 10 A/dm^2; (b) 30 A/dm^2

4. CONCLUSIONS

Ni–Fe–P–CeO$_2$ composite coatings were prepared on a #45 steel substrate using jet electrodeposition technology at different processing current densities to investigate the effect of current density on the coating performance. First, the surface micro-morphology, microhardness, structure, and structural components of the composite coating were analyzed. Subsequently, the wear and corrosion resistances of the composite coating were studied. The following conclusions can be drawn from the results:

(1) The surface of the Ni–Fe–P–CeO$_2$ composite coating prepared by jet electrodeposition technology exhibited a typical cell structure. As the current density increased, the flatness and density of the composite coating surface were improved. When the current density was increased to 30 A/dm^2, the grains were refined, there were fewer attached particles, the cell structure was compact, the density was good, and the coating surface was flat.

(2) The Ni–Fe–P–CeO_2 composite coating exhibited an amorphous structure. Increasing the current density facilitated the agglomeration of the nano-CeO_2 particles, weakened the inhibitory effect of Fe^{2+} on the reduction process of Ni^{2+}, and promoted the co-deposition rate of Fe, Ni, and P, which helped evenly distribute the nano-CeO_2 particles and various elements on the coating. When the current density was 30 A/dm^2, the elements in the Ni–Fe–P–CeO_2 composite coating were evenly distributed.

(3) With increasing current density, the crystal grains were refined, and under the effect of dispersion strengthening of the nano-CeO_2 particles, the microhardness of the composite coating first increased and then decreased. At a current density of 30 A/dm^2, the microhardness of the composite coating reached a maximum value of 614.24 $HV_{0.1}$.

(4) With increasing current density, the width, depth, and cross-sectional area of the wear scar on the coating surface decreased first and then increased. At low current densities, significant peeling marks and cracks were observed on the wear scars, accompanied by serious adhesion and wear. With the increase in the current density, the large amount of peeling off at the wear interface was improved. When the current density was 30 A/dm^2, the width, depth, and cross-sectional area of the wear scar were the lowest, and the wear resistance performance was the best.

(5) Compared with the composite coating prepared at low current densities, the Ni–Fe–P–CeO_2 coating prepared at a high processing current density exhibited a higher self-corrosion potential, lower self-corrosion current, higher charge transfer resistance, and lower corrosion efficiency. When the current density increased to 30 A/dm^2, the prepared composite coating exhibited the highest self-corrosion potential, lowest self-corrosion current, highest charge transfer resistance, low corrosion efficiency, and excellent corrosion resistance.

ACKNOWLEDGEMENTS

Supported by the Fundamental Research Funds for the Central Universities (Grant number KYXJ202002), the China Postdoctoral Science Foundation (Grant number 2017M621665), the Postdoctoral Science Foundation of Jiangsu Province of China (Grant number 2018K022A)

References

1. H. Gül, F. Kılıç, M. Uysal, S. Aslan, A. Alp and H. Akbulut, *Appl. Surf. Sci.,* 258(2012)4260.
2. W. W. Zhang, C. C. Ji and B. S. Li, *Results Phys.*, 13(2019)102242.
3. N. S. Nia, J. Creus, X. Feaugas and C. Savall, *Appl. Surf. Sci.*, 370(2016)149.
4. B. S. Li, D. D. Li, T. Y. Mei, W. Z. Xia and W. W. Zhang, *J. Alloys Compd.*, 777(2019)1234.
5. A. K. Chaudhari and V.B. Singh, *J. Alloy. Compd.*, 751 (2018) 194.
6. J. M. Costa, M. S. Hori and A. F.de Almeida Neto, *Chem. Phys.*, 527 (2019) 110502.
7. R. Mishra and R. Balasubramaniam, *Corros. Sci.*, 46 (2004) 3019.
8. E. Yousefi, S. Sharafi and A. Irannejad, *J. Alloy. Compd.*, 753 (2018) 308.
9. V. S. Kathavate, D. N. Pawar, N. S. Bagal and P. P. Deshpande, *J. Alloy. Compd.*, 823 (2020) 153812.
10. P. Wang, S. J. Deng, Y. D. He, C. X. Liu and J. Zhang, *Corros. Sci.*, 109(2016)13.
11. Z. H. Chen, G. J. Shao, Z. P. Ma, J. J. Song, G. L. Wang and W. W. Huang, *Mater. Lett.*, 160 (2015) 34.
12. A. Sanaty-Zadeh, K. Raeissi and A. Saidi, *J. Alloy. Compd.*, 485 (2009) 402.
13. G. P. Pavithra, A. C. Hegde, *Appl.Surf. Sci.*, 258 (2012) 6884.

14. N. P. Wasekar, P. Haridoss, S. K. Seshadri and G. Sundararajan, *Surf. Coat. Technol.*, 291 (2016)130.
15. R. P. Edavan and R. Kopinski, *Corros. Sci.*, 51(2009)2429.
16. T. F. Xiang, M. X. Zhang, C. Li, C. D. Dong, L. Yang and W. M. Chan, *J. Alloy. Compd.*, 736 (2018)62.
17. C. Wang, L. D. Shen, M. B. Qiu, Z. J. Tian and W. Jiang, *J. Alloy. Compd.*, 727(2017)269.
18. R. Sen, S. Das and K. Das, *Surf. Coat. Technol.*, 205(2011)3847.
19. B. S. Li and W. W. Zhang, *J. Alloy. Compd.*, 820(2020)153158.
20. V. K. Sharma and V. Kumar, *J. Mater. Res. Technol-JMRT*, 8(2019)1971.
21. T. K. Mishra, A. Kumar, S. K. Sinha and B. Gupta, *Mater. Today:. Proc.*, 5(2018)27786.
22. S. T. Sun, H. G. Fu, X. L. Ping, X. Y. Guo, J. Lin, Y. P. Lei, W. B. Wu and J. X. Zhou, *Surf. Coat. Technol.*, 359(2019)300.
23. Y. Q. Li, H. W. Shang, Y. H. Zhang, P. Li, Y. Qi and D. L. Zhao, *Int. J. Hydrogen Energy*, 44(2019)1735.
24. P. I. Nemes, M. Lekka, L. Fedrizzi and L. M. Muresan, *Surf. Coat. Technol.*, 252(2014)102.
25. S. T. Aruna, C. N. Bindu, V. E. Selvi, V. K. W. Grips and K. S. Rajam, *Surf. Coat. Technol.*, 200(2006)6871.
26. D. N. Sangeetha, R. S. Holla, B. R. Bhat and M. Selvakumar, *Int. J. Hydrogen Energy*, 45(2020)7801.
27. H. L. Jia, C. Y. Zou, J. X. Wu, X. Tan and M. Li, *Physica B*, 585(2020)412060.
28. A. M. Rashidi and A. Amadeh, *Surf. Coat. Technol.*, 202(2008)3772.
29. X. Y. Cuan, J. Pan, R. Q. Cao, Y. Lin, J. H. Yao, Y. X. Wang and Y. Li, *Mater. Lett.*, 218(2018)150.
30. N. Bhadauria, S. Pandey and P. M. Pandey, *Materials Today: Proceedings*, (2020)2986.
31. S. E. Hadian and D. R. Gabe, *Surf. Coat. Technol.*, 122(1999)118.
32. P. Peng, *J. Alloy. Compd.*, 821(2020)155002.
33. D. Thiemig, A. Bund and J. B. Talbot, *Electrochim. Acta,*5 4(2009)2491.
34. B. H. Chen, S. G. Liu, P.F. Ji, B. Li, X. Y. Zhang, M. Z. Ma and R. P. Liu, *J. Alloys Compd.*, 831(2020)154839.
35. C. Guo, Y. Zuo, X. H. Zhao, J. M. Zhao, J. P. Xiong, *Surf. Coat. Technol.*, 202(2008)3246.
36. J. Wei, P. Guo, L. L. Liu, H. C. Li, H. Li, S. Y. Wang, Peiling Ke, Hidetoshi Saito and Aiying Wang, *Electrochim. Acta*, 346(2020)136282.
37. J. K. Pancrecious, J. P. Deepa, V. Jayan, U. S. Bill, T. P. D. Rajan and B. C. Pai, *Surf. Coat. Technol.*, 356(2018)29.
38. K. Aggoun, L. Chaal, J. Creus, R. Sabot, B. Saidani and M. Jeannin, *Surf. Coat. Technol.*, 372(2019)410.
39. M. R. Dayyari, A. Amadeh and S. Sadreddini, *Mater. Chem. Phys.*, 199(2017)537.
40. L. L. Guo, Q. Liu, H. Q. Yin, T. J. Pan and Z. F. Tang, *Corros. Sci.*, 166(2020)108473.
41. M. Isakhani-Zakaria, S. R. Allahkaram and H. A. Ramezani-Varzaneh, Corros. Sci., 157(2019)472.
42. S. Khorsand, K. Raeissi and F. Ashrafizadeh, *Appl. Surf. Sci.*, 305(2014)498.
43. M. Rahsepar and M. E. Bahrololoom, *Corros. Eng., Sci. Technol.*, 46(2011)70.
44. X. L. Ji, C. Y. Yan, H. Duan and C. Y. Luo, *Surf. Coat. Technol.*, 302(2016) 208.